

Electromechanical Properties of Graphene Drumheads

Nikolai N. Klimov *et al.*
Science **336**, 1557 (2012);
DOI: 10.1126/science.1220335

This copy is for your personal, non-commercial use only.

If you wish to distribute this article to others, you can order high-quality copies for your colleagues, clients, or customers by [clicking here](#).

Permission to republish or repurpose articles or portions of articles can be obtained by following the guidelines [here](#).

The following resources related to this article are available online at www.sciencemag.org (this information is current as of June 21, 2012):

Updated information and services, including high-resolution figures, can be found in the online version of this article at:

<http://www.sciencemag.org/content/336/6088/1557.full.html>

Supporting Online Material can be found at:

<http://www.sciencemag.org/content/suppl/2012/06/20/336.6088.1557.DC1.html>

This article cites 24 articles, 3 of which can be accessed free:

<http://www.sciencemag.org/content/336/6088/1557.full.html#ref-list-1>

This article appears in the following subject collections:

Physics, Applied

http://www.sciencemag.org/cgi/collection/app_physics

$\lambda_L^2(0)$ does appear to be enhanced in heavy-fermion superconductors, which contain interacting conduction electrons and local moments (25, 26). The present results in BaFe₂(As_{1-x}P_x)₂ support this and suggest that in sufficiently clean systems electron correlation effects can lead to a striking renormalization of $\lambda_L^2(0)$.

We now discuss the consequences of a QPT inside the superconducting dome. Such a QPT implies that the non-Fermi liquid behavior indicated by the red region in Fig. 2A is most likely associated with a finite temperature quantum critical region linked to the QCP. Moreover, this transition immediately indicates two distinct superconducting ground states. In our system, the robust T -linear behavior of $\delta\lambda_L(T)$ on both sides of the purported QCP at $x = 0.30$ argues against a drastic change in the superconducting gap structure (2, 6). The fact that the zero-temperature extrapolation of the antiferromagnetic transition $T_N(x)$ into the dome (12) coincides with the location of the QCP (Fig. 2A) may indicate that the QCP separates a pure superconducting phase on the right and a superconducting phase coexisting with spin-density-wave (SDW) order on the left (Fig. 1B).

To place BaFe₂(As_{1-x}P_x)₂ in the context of other superconductors, we plotted T_c as a function of the effective Fermi temperature T_F for several types of compounds (Uemura plot, Fig. 4); the red symbols correspond to various values of x for BaFe₂(As_{1-x}P_x)₂ studied here, and the others are obtained from μ SR measurements reported previously (27). Because the relevant Fermi surface sheets are nearly cylindrical, T_F for two-dimensional (2D) systems may be estimated directly from $\lambda_L(0)$ via the relation

$$T_F = \frac{(\hbar^2 \pi) n_{2D}}{k_B m^*} \approx \left(\frac{\hbar^2 \pi}{\mu_0 e^2 d} \right) \lambda_L^2(0),$$

where n_{2D} is the carrier concentration within the superconducting planes and d is the interlayer spacing; $T_F = (\hbar^2/2)(3\pi^2)^{2/3} n^{2/3}/k_B m^*$ for 3D systems (27). The dashed line corresponds to the Bose-Einstein condensation (BEC) temperature for an ideal 3D boson gas, $T_B = \frac{\hbar^2}{2\pi m^* k_B} \left(\frac{n}{2.612} \right)^{2/3}$. In a

quasi-2D system, this value of T_B provides an estimate of the maximum condensate temperature. The evolution of T_c with T_F in the present system is in sharp contrast to that in cuprates, in which T_c is roughly scaled by T_F . The inset of Fig. 4 depicts the x -composition dependence of T_c normalized by Fermi (or BEC) temperature, T_c/T_F (T_c/T_B). In the large composition region ($x > 0.6$), T_c/T_F is very small, comparable to that of the conventional superconductor Nb. As x is decreased, T_c/T_F increases rapidly and then decreases in the SDW region after reaching the maximum at the QCP ($x = 0.30$). Notably, the magnitude of T_c/T_B (≈ 0.30) at the QCP exceeds that of cuprates and reaches almost 40% of the value of superfluid 4 He.

The fact that T_c/T_F becomes largest at the QCP indicates that the strongest pairing interaction is achieved at the QCP, implying that

high- T_c superconductivity is driven by the QCP. In a multiband system, we need to introduce the effective Fermi energy ϵ_F for each band, which is defined for electron bands as the energy of the highest occupied state relative to the top of the band and for hole bands as the energy of the highest occupied state relative to the bottom of the band. Because the outer electron sheet with the highest Fermi velocity has the largest ϵ_F and hence the largest contribution to $\lambda_L^2(0)$, the magnitudes of T_c/T_F in the other sheets are expected to be even larger. These results lead us to consider that in terms of T_c/T_F the system is closer to the Bardeen-Cooper-Schrieffer-BEC crossover (28–30) than the cuprates.

References and Notes

1. G. R. Stewart, *Rev. Mod. Phys.* **83**, 1589 (2011).
2. P. J. Hirschfeld, M. M. Korshunov, I. I. Mazin, *Rep. Prog. Phys.* **74**, 124508 (2011).
3. M. R. Norman, D. Pines, C. Kallin, *Adv. Phys.* **54**, 715 (2005).
4. J. Dai, Q. Si, J.-X. Zhu, E. Abrahams, *Proc. Natl. Acad. Sci. U.S.A.* **106**, 4118 (2009).
5. D. M. Broun, *Nat. Phys.* **4**, 170 (2008).
6. R. M. Fernandes, J. Schmalian, *Phys. Rev. B* **82**, 014521 (2010).
7. See, for example, S. Sachdev, B. Keimer, *Phys. Today* **64**, 29 (2011).
8. See supplementary materials on *Science* Online.
9. E. G. Moon, S. Sachdev, *Phys. Rev. B* **80**, 035117 (2009).
10. H. Shishido *et al.*, *Phys. Rev. Lett.* **104**, 057008 (2010).
11. S. Kasahara *et al.*, *Phys. Rev. B* **81**, 184519 (2010).
12. Y. Nakai *et al.*, *Phys. Rev. Lett.* **105**, 107003 (2010).
13. R. Prozorov, R. W. Giannetta, *Supercond. Sci. Technol.* **19**, R41 (2006).
14. R. T. Gordon *et al.*, *Phys. Rev. B* **82**, 054507 (2010).
15. R. Prozorov, V. G. Kogan, *Rep. Prog. Phys.* **74**, 124505 (2011).
16. K. Hashimoto *et al.*, *Phys. Rev. B* **81**, 220501(R) (2010).
17. M. Yamashita *et al.*, *Phys. Rev. B* **84**, 060507(R) (2011).

18. C. Chaparro *et al.*, Doping dependence of the specific heat of single crystal BaFe₂(As_{1-x}P_x)₂ (2011); <http://arxiv.org/abs/1110.3075>.
19. S. L. Bud'ko, N. Ni, P. C. Canfield, *Phys. Rev. B* **79**, 220516(R) (2009).
20. J. Zaanen, *Phys. Rev. B* **80**, 212502 (2009).
21. L. Luan *et al.*, *Phys. Rev. Lett.* **106**, 067001 (2011).
22. J. L. Tallon, J. W. Loram, J. R. Cooper, C. Panagopoulos, B. Bernhard, *Phys. Rev. B* **68**, 180501 (2003).
23. C. Panagopoulos *et al.*, *Phys. Rev. B* **66**, 064501 (2002).
24. A. J. Leggett, *Phys. Rev.* **140**, A1869 (1965).
25. C. M. Varma, K. Miyake, S. Schmitt-Rink, *Phys. Rev. Lett.* **57**, 626 (1986).
26. F. Gross *et al.*, *Z. Phys. B* **64**, 175 (1986).
27. Y. J. Uemura, *J. Phys. Condens. Matter* **16**, S4515 (2004).
28. Q. Chen, J. Stajic, S. Tan, K. Levin, *Phys. Rep.* **412**, 1 (2005).
29. C. Sá de Melo, M. Randeria, J. R. Engelbrecht, *Phys. Rev. Lett.* **71**, 3202 (1993).
30. Y. J. Uemura, *Physica B* **404**, 3195 (2009).

Acknowledgments: We thank R. M. Fernandes, S. Kivelson, H. Kontani, Q. Si, U. Welp, and Y. Yanase for valuable discussion. Supported by Grant-in-Aid for the Global Centers of Excellence program “The Next Generation of Physics, Spun from Universality and Emergence,” Grant-in-Aid for Scientific Research on Innovative Areas “Heavy Electrons” from the Ministry of Education, Culture, Sports, Science and Technology of Japan, KAKENHI from Japan Society for the Promotion of Science, and the Engineering and Physical Sciences Research Council (UK). Work at the Ames Laboratory was supported by the U.S. Department of Energy, Basic Energy Sciences, Materials Science and Engineering Division, under contract no. DE-AC02-07CH11358. Work at the University of Illinois was supported by the Center for Emergent Superconductivity, an Energy Frontier Research Center funded by the U.S. Department of Energy, Office of Science, Office of Basic Energy Sciences under award no. DE-AC0298CH1088.

Supplementary Materials

www.sciencemag.org/cgi/content/full/336/6088/1554/DC1
Materials and Methods
Supplementary Text
Figs. S1 to S5
References (31–42)

30 January 2012; accepted 10 May 2012
10.1126/science.1219821

Electromechanical Properties of Graphene Drumheads

Nikolai N. Klimov,^{1,2,3} Suyong Jung,^{1,2,*} Shuze Zhu,⁴ Teng Li,^{2,4}† C. Alan Wright,⁴ Santiago D. Solares,^{2,4}† David B. Newell,³ Nikolai B. Zhitenev,¹ Joseph A. Stroscio¹†

We determined the electromechanical properties of a suspended graphene layer by scanning tunneling microscopy (STM) and scanning tunneling spectroscopy (STS) measurements, as well as computational simulations of the graphene-membrane mechanics and morphology. A graphene membrane was continuously deformed by controlling the competing interactions with a STM probe tip and the electric field from a back-gate electrode. The probe tip-induced deformation created a localized strain field in the graphene lattice. STS measurements on the deformed suspended graphene display an electronic spectrum completely different from that of graphene supported by a substrate. The spectrum indicates the formation of a spatially confined quantum dot, in agreement with recent predictions of confinement by strain-induced pseudomagnetic fields.

Suspending graphene sheets can remove unwanted electrical potential disturbances from supporting substrates. Initial measurements of graphene devices on SiO₂ insulating substrates achieved carrier mobilities of $\approx 5000 \text{ cm}^2 \text{ V}^{-1} \text{ s}^{-1}$ (1). Removing the substrate by suspending graphene resulted in mobilities in excess of $200,000 \text{ cm}^2 \text{ V}^{-1} \text{ s}^{-1}$ at low temperatures

(2). These differences illustrate how substrate-induced potential disorder due to impurities and strain can play a role in the electronic properties of graphene. Recently, strain engineering of the electronic properties of graphene, which can be described through the generation of local pseudoscalar and magnetic fields by strain (3–11), has attracted considerable attention. For example,

strain-generated pseudomagnetic fields equivalent to a real magnetic field as high as 300 T have been reported (5). However, a number of questions remain regarding the structure and electronic properties of suspended graphene layers.

In this Report, we present scanning tunneling microscopy (STM) and scanning tunneling spectroscopy (STS) measurements of suspended graphene drumheads in a back-gated graphene device structure. We achieved stable STM measurements on the suspended graphene by carefully approaching the membrane with very slow scanning speeds. We observed that both the van der Waals forces from the STM probe tip and electrostatic force induced by back-gate voltage can induce substantial mechanical deformation in the suspended graphene membranes. The visible membrane shape measured as a tip height can be continuously tuned from concave to convex by adjusting the electrostatic force. However, the induced strain in the graphene membrane mainly originates from the tip-membrane interaction, dramatically altering the electronic spectrum of graphene compared with the measurements of graphene directly supported by a substrate (12, 13). In particular, we observed multiple quartet bands of peaks in the differential conductance spectra that are characteristic of charge confinement in a quantum dot (QD). Theoretical simulations of the membrane mechanics and experimental results confirm recent predictions of QD confinement in pseudomagnetic fields generated by rotationally symmetric strain fields in graphene membranes (6, 7).

Figure 1, A to C, shows the geometry of the graphene device we used in this study. We fabricated an array of pits in SiO_2/Si substrates, 1.1 μm in diameter and 100 nm in depth, by shallow plasma etching of SiO_2 (Fig. 1C). Graphene flakes were exfoliated onto the prepatterned SiO_2/Si substrate via mechanical exfoliation of natural graphite and contacted using a Pd/Au electrode deposited via a stencil mask (Fig. 1B). After fabrication, we aligned the STM probe tip onto the device in ultrahigh vacuum by using an external optical microscope before cooling the STM module in a custom STM system operating at 4 K (14).

STM topographic images of single-layer supported and suspended graphene over an area of 20 nm by 20 nm are shown in Fig. 1, D and E, respectively. On small length scales, the graphene honeycomb lattice was clearly resolved on both supported and suspended graphene, with compa-

rable corrugation amplitudes (Fig. 1, D and E, insets). On the 20-nm length scale, the peak-to-peak height corrugation on the suspended graphene was about four times larger than that of the supported graphene on the SiO_2 substrate over this scan area range (Fig. 1F). The larger height variation on the graphene membrane indicates deformation of the graphene sheet, which becomes larger with greater scan sizes (Fig. 2).

To obtain STM images of suspended graphene, as in Fig. 1E, we had to approach the suspended graphene area from the supported edge at very low scan speed to avoid exciting the graphene drumhead. If the drumhead was excited, the STM servo loop would go into oscillation with uncontrolled amplitude. However, when the scan speed was kept sufficiently low, a large continuous deformation of the graphene membrane could

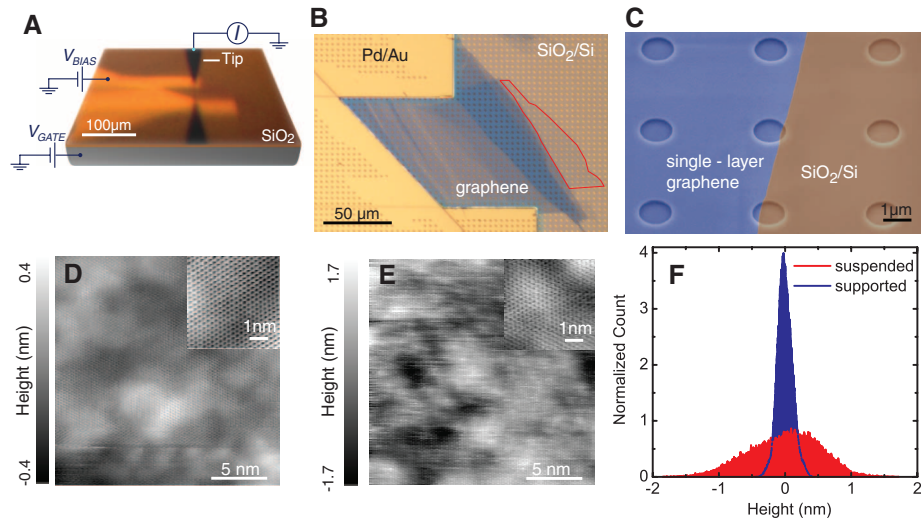


Fig. 1. STM measurements of graphene drumheads. (A) Optical image of the gated graphene device. The device consists of a single graphene layer placed over an array of pits (1.1 μm in diameter, 100 nm in depth) etched in SiO_2 (300 nm)/ Si substrate. (B) Magnified optical image of the device in (A). The single-layer graphene region is denoted by a red outline. (C) Scanning electron microscope image of the device. STM topographic images, 20 by 20 nm, on the supported graphene (D) and suspended graphene membrane (E). Insets show the graphene atomic lattice images (5 by 5 nm). The inset gray scales cover the range of ± 0.2 nm. (F) Topographic height histograms from the images in (D) and (E).

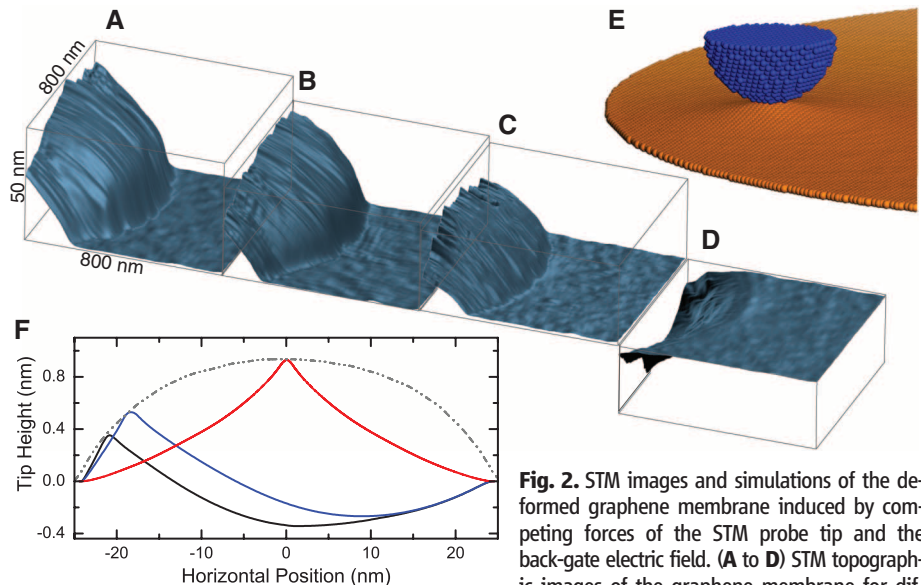


Fig. 2. STM images and simulations of the deformed graphene membrane induced by competing forces of the STM probe tip and the back-gate electric field. (A to D) STM topographic images of the graphene membrane for different gate voltages: 0 V (A), 20 V (B), 40 V (C), and 60 V (D). The membrane is deformed by upward forces from the STM tip and a downward force due to the electric field from the applied V_{GATE} . (E) Atomistic model showing deformations in the graphene membrane interacting with the STM tip. The radii of the tip and membrane in this model are 2.5 and 25 nm, respectively. (F) Calculated membrane shapes at the critical tip height for horizontal tip positions of 2.5 nm (black curve), 5.2 nm (blue curve), and 25 nm (red curve) from the membrane edge. A back-gate force of 0.012 pN was applied to each atom in the membrane. The gray dot-dashed curve is an envelope showing the membrane height as seen in a STM measurement.

¹Center for Nanoscale Science and Technology, National Institute of Standards and Technology (NIST), Gaithersburg, MD 20899, USA. ²Maryland NanoCenter, University of Maryland, College Park, MD 20742, USA. ³Physical Measurement Laboratory, NIST, Gaithersburg, MD 20899, USA. ⁴Department of Mechanical Engineering, University of Maryland, College Park, MD 20742, USA.

*Present address: Korea Research Institute of Standards and Science, Daejon, Republic of Korea.

†To whom correspondence should be addressed. E-mail: ssolares@umd.edu (S.D.S.); lit@umd.edu (T.L.); joseph.strosio@nist.gov (J.A.S.)

be observed as the tip scanned the graphene suspended over the pits in the substrate (Fig. 2, A to D). This visible deformation could be continuously tuned to be either positive (outward from the surface, Fig. 2, A to C) or negative (inward to the surface, Fig. 2D), depending on the magnitude of the voltage, V_{GATE} , applied to the back-gate electrode.

The graphene deformation in Fig. 2, A to D, was caused by the STM probe tip pulling up on the membrane via the van der Waals and electrostatic forces and the back-gate electrode pulling the membrane down via electrostatic force. In the progression of images from Fig. 2, A to D, the force from the back gate was incrementally increased as V_{GATE} was changed from 0 to 60 V, which progressively pulled the membrane downward. Between 50 and 60 V, the forces from the probe tip were balanced by the gate field, and finally at 60 V, the force from the back gate pulled the graphene into the underlying pit. In contrast, a tip-membrane potential difference in the range of ± 1 V and the related electrostatic force produced only a small effect on the membrane

shape, implying that the van der Waals force between the probe tip and graphene membrane is the dominant pull-up force. We also augmented our spectroscopic measurements with molecular dynamics simulations discussed below.

To study the electronic properties of the suspended graphene membranes, we applied gate-mapping STS measurements at high resolution in which individual dI/dV spectra (where I is current) are measured at a fixed spatial location as a function of both tunneling bias, V_B , and back-gate voltage, V_{GATE} (Fig. 3) (12, 15). The dI/dV spectra, proportional to the local density of states, were used to examine how the suspension of the graphene affects its electronic spectrum. The electronic spectrum of graphene in a uniform applied magnetic field, B , consists of a set of quantized Landau levels (LLs) (16, 17). Gate-mapping measurements made on the suspended membrane at the same fixed location (Fig. 3, A to D) show a graphene electronic spectrum dramatically different from the measurements on supported graphene layers (12, 13). The notable signatures of the spectra of supported graphene [see (12, 13)]

are the following: (i) In zero applied magnetic field, tunneling spectra show a minimum at the Dirac point with its distinct square-root dispersion as a function of density (18), and (ii) in applied magnetic fields, magnetically quantized LLs form a staircase pattern in the gate maps as the LLs are sequentially pinned at the Fermi level. Spectra are very different on the suspended membrane. In zero applied magnetic field, the dI/dV gate map (Fig. 3A) showed a new series of states seen as lines with a small negative slope with increasing gate voltage (almost horizontal across the gate map). In addition, we observed a series of broad bands with positive slopes, as indicated with the blue arrows in Fig. 3A. These latter features with positive slopes became more resolved in an applied magnetic field, seen at $B = 5$ T (Fig. 3B) and 8 T (Fig. 3, C and D), resembling the spectral signatures of QDs (12, 19). [See supplemental data (18) for a comparison of the gate maps on supported and suspended graphene].

To further explore the analogy with QD physics, we examine the energy scales in the spectral maps of the suspended graphene. As an example,

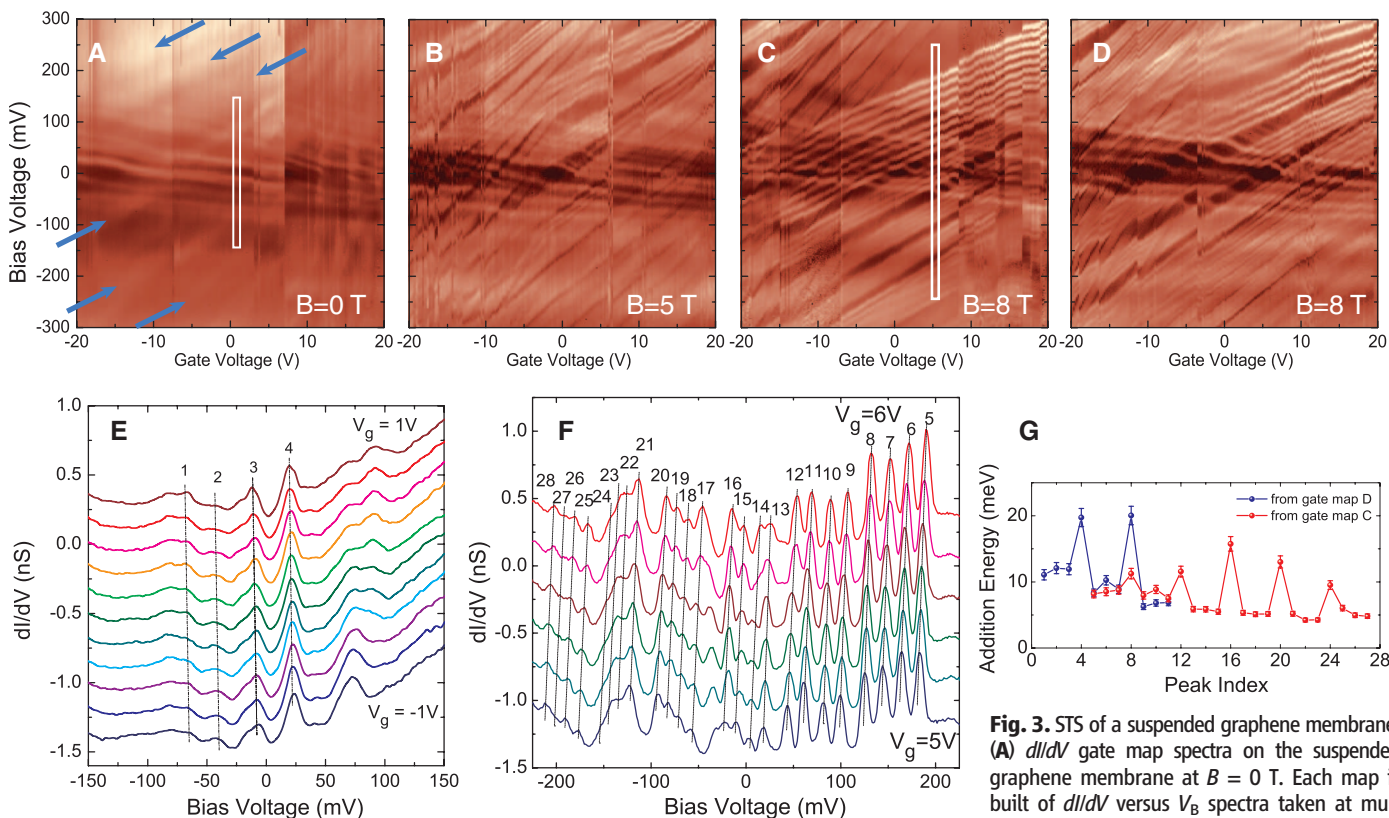


Fig. 3. STS of a suspended graphene membrane. (A) dI/dV gate map spectra on the suspended graphene membrane at $B = 0$ T. Each map is built of dI/dV versus V_B spectra taken at multiple fixed gate voltages. The color scale is the

dI/dV magnitude, which varies from 0.05 nS (dark) to 1.7 nS (bright) for (A) and to 1.2 nS (bright) for (B) to (D). The blue arrows indicate spectral bands with positive slope that become more resolved at higher fields in (B) and (C). (B and C) dI/dV gate-map spectra on the suspended graphene membrane at (B) $B = 5$ T and (C) $B = 8$ T. The white rectangle in (C) denotes the region where individual spectra are obtained and plotted in (F). (D) dI/dV gate-map spectra at $B = 8$ T, showing the variability in the measurements when moving off and back on the membrane. (E) dI/dV versus V_B spectra from the $B = 0$ T gate map in (A) for gate voltages varying from -1 to 1 V. (F) dI/dV versus V_B spectra from the $B = 8$ T gate map in (C) for gate voltages varying from 5 to 6 V. The spectra are shifted vertically for clarity in (E) and (F). (G) QD addition energies corresponding to the difference in dI/dV peak positions in the spectra from the gate maps in (C) (red symbols) and (D) (blue symbols). Energies are converted from bias voltages using the lever arm, $E = \alpha V_B$, where $\alpha = 0.45 \pm 0.03$. The error bars in (G) are dominated by the statistical error in α , which was determined from 1-SD uncertainties in the measured slopes of the charging lines in the gate maps. These uncertainties, in turn, determine the corresponding uncertainties in the capacitance ratios discussed in the main text.

dI/dV spectra that are part of the gate maps in Fig. 3, A and C, are shown in Fig. 3, E and F, respectively. The peaks in Fig. 3E corresponding to the horizontal lines in the zero-field gate map (Fig. 3A) showed a separation of ≈ 30 mV for the first few states. In contrast, the peaks in Fig. 3F that form the positive-slope bands were seen in groups of four with a spacing of ≈ 20 mV. This grouping is similar to the fourfold charging peaks in QDs observed in graphene (12) or carbon nanotubes (19) and reflects the fourfold degeneracy of the dot levels caused by electron spin and valley quantum numbers. These dI/dV peaks are caused by an opening up of a transport channel at the Fermi energy associated with a single-electron addition to the QD. The peaks appeared as tilted lines in the map because the QD energy levels are controlled by a linear combination of the gate voltage and tip bias.

Here, we use this analogy to determine the energy scale and the size of the QD from the measured slopes and spacing of the charging lines. The vertical voltage bias axis is converted to the QD energy spacing using the lever arm, $E = \alpha V_B$, where $\alpha = C_B/C_T \approx 0.4$, C_B is the graphene layer to graphene QD capacitance, and

C_T is the total capacitance of the QD. In Fig. 3G, we plot the energy difference between the levels from the gate maps in Fig. 3, C and D (red and blue symbols, respectively). The energy spacing of the individual levels follows the classic energy spectrum of a QD (20), $e^2/C_T + \Delta E_{N+1}$, where e is the charge on an electron, e^2/C_T is the charging energy of the fourfold degenerate levels of a graphene QD (base line in Fig. 3G), and the additional energy, $\Delta E_{N+1} = \Delta E_{N+1} - \Delta E_N$, separating each band (spikes in Fig. 3G) corresponds to the energy needed to reach the next QD level (where N is the current quantum level). The charging energies, varying from 11.7 ± 0.5 to 5.3 ± 0.7 meV in Fig. 3G, correspond to QDs with diameters in a range from 34 ± 2 to 53 ± 5 nm (21). This dot size is consistent with a simple estimate based on the number of electrons added to the dot for a given range of gate voltage. In the gate map (Fig. 3C), we see approximately five quartet bands over the gate-voltage range of 40 V, corresponding to the addition of 20 electrons to the QD. The gate capacitance of 5.85 nF cm^{-2} (100-nm vacuum plus 200-nm oxide) yields a rough estimate of the dot diameter of 42 nm.

The profile of the membrane as measured by the tip height cannot explain the formation of a QD. To understand the local and global membrane deformation and the corresponding strain induced in the immediate vicinity of the STM tip, we performed molecular dynamics simulations (18). The calculations involved approaching the membrane with the tip at three different horizontal locations along a radial line across the membrane (2.5 and 5.2 nm from the edge, as well as in the center of the membrane) and then retracting the tip until a critical point was reached, at which further retraction of the tip would result in loss of tip-membrane contact (18). This critical point simulates the action of the STM servo that redraws the tip from the membrane to avoid contact while it maintains a vacuum tunneling gap. Additionally, a constant force of magnitude in the range 0 to 0.06 pN was applied to each carbon atom of the membrane to simulate the electrostatic force exerted by the gate electrode. The range of the back-gate force was selected such that different levels of membrane deformation took place above and below the neutral position (fig. S9) (18).

Figure 2E illustrates the atomistic model that we used, showing the tip at the critical height above the pulled-up membrane. In Fig. 2F, the membrane shapes at the critical tip height are plotted together for three tip locations on a membrane, for a back-gate force of 0.012 pN per atom. The computational simulations show that the deformation in the graphene membrane induced by the probe tip is formed locally. The simulations further demonstrate that the measured membrane profiles are not caused by a static membrane deformation, but one that continuously changes with the tip position. As the STM tip is rastered across a membrane, the cusp of the deformation follows the tip (Fig. 2F), and the

domelike shapes recorded in STM images (Fig. 2, A to D) are the envelopes tracing the cusp peak, as illustrated by the dot-dashed line in Fig. 2F.

The mechanical simulations also show that the deformation in the graphene lattice induced a strain in the membrane (Fig. 4A), which was localized on the small scale of the probe-tip diameter (5 nm) used in the simulation. A scaling analysis (figs. S12 and S13) (18) shows the deformation area scales with the square root of the probe-tip diameter for a flat membrane. Extrapolating the deformation size for the experimental probe diameter of 100 nm (determined by scanning electron microscopy) yields a strain field diameter of ≈ 23 nm for the current experiment. Because the local deformation of the membrane under the tip does not change substantially as the probe tip moved across the membrane (Fig. 2F), the local strain field is fairly constant at all tip positions. The local deformation is also expected to be fairly independent of gate voltage, because the cusp of the deformation is controlled largely by the van der Waals force from the probe tip (fig. S9) (18).

Peak areal strains up to $\approx 1\%$ are predicted (Fig. 4A) in the graphene lattice directly under the tip. This strain produces pseudofields that could directly affect the graphene charge carriers (3–11). The symmetry of the pseudofields is determined by the corresponding symmetry of the strain field. For example, a uniform pseudomagnetic field requires a special strain field (4) distorted with threefold symmetry. In our case, a rotationally symmetric strain field generates a threefold pseudomagnetic field with alternating signs (6, 7). Figure 4B shows the calculated pseudomagnetic field for the strain field in Fig. 4A for the suspended membrane resulting in alternating spatial fields of ± 10 T. The region where the pseudofield is maximal is ≈ 10 nm in diameter for the 50-nm membrane diameter used in the simulation. The use of the same scaling as described above results in an effective pseudofield diameter of ≈ 45 nm (18).

Carriers in graphene can penetrate large potential barriers due to the effect of Klein tunneling (22), and physical barriers are typically engineered (23) to confine carriers. The pseudomagnetic field spatially confines the graphene carriers curving the classical trajectories and forming clockwise and counterclockwise orbits around the alternating peaks of the pseudomagnetic field (6, 7). However, some electronic states corresponding to classic snake orbits that propagate along the lines where the pseudomagnetic field changes sign will not be confined. We suggest that the application of an external magnetic field suppresses such leaky orbits by canceling one component of the pseudomagnetic field that opposes the applied magnetic field, which improves the overall confinement, as observed in Fig. 3, B to D. The dot size estimated from the charging energies in the gate maps (Fig. 3G) is ≈ 34 to 53 nm in diameter, which is in reasonable

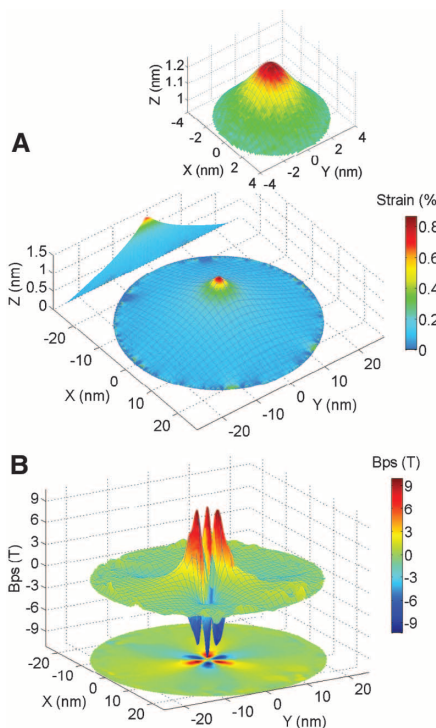


Fig. 4. Simulations of a graphene membrane shape and corresponding strain and pseudomagnetic field. (A) Graphene membrane shape with the STM tip positioned over the center of the membrane at zero back-gate force. The inset shows a zoomed-in region where the strain is maximal. The radii of the tip and membrane in this model are 2.5 and 25 nm, respectively. (B) The pseudomagnetic field, calculated from the strain in (A) (fig. S10) (18), shows a spatially alternating field with threefold symmetry that can spatially confine carriers.

agreement with the size of the estimated pseudofield (45 nm). The density-of-states peaks observed as weakly negative sloping lines in the gate maps (Fig. 3A) may be caused by localization in a spatially varying pseudofield (6, 7, 10), although a detailed model is currently not available. The variations in positive-slope bands (Fig. 3, B to D) are probably caused by minor deformations of the overall membrane shape affecting the size of the QD.

References and Notes

- K. S. Novoselov *et al.*, *Proc. Natl. Acad. Sci. U.S.A.* **102**, 10451 (2005).
- K. I. Bolotin *et al.*, *Solid State Commun.* **146**, 351 (2008).
- M. M. Fogler, F. Guinea, M. I. Katsnelson, *Phys. Rev. Lett.* **101**, 226804 (2008).
- F. Guinea, M. I. Katsnelson, A. K. Geim, *Nat. Phys.* **6**, 30 (2010).
- N. Levy *et al.*, *Science* **329**, 544 (2010).
- K.-J. Kim, Y. M. Blanter, K.-H. Ahn, *Phys. Rev. B* **84**, 081401 (2011).
- G. M. M. Wakker, R. P. Tiwari, M. Blaauboer, *Phys. Rev. B* **84**, 195427 (2011).
- F. Guinea, B. Horovitz, P. Le Doussal, *Phys. Rev. B* **77**, 205421 (2008).
- F. Guinea, A. K. Geim, M. I. Katsnelson, K. S. Novoselov, *Phys. Rev. B* **81**, 035408 (2010).
- T. O. Wehling, A. V. Balatsky, A. M. Tsvelik, M. I. Katsnelson, A. I. Lichtenstein, *Europhys. Lett.* **84**, 17003 (2008).
- M. Gibertini, A. Tomadin, M. Polini, *Phys. Rev. B* **81**, 125437 (2010).
- S. Jung *et al.*, *Nat. Phys.* **7**, 245 (2011).
- A. Luican, G. Li, E. Y. Andrei, *Phys. Rev. B* **83**, 041405 (2011).
- J. A. Stroscio, E. W. Hudson, S. R. Blankenship, R. J. Celotta, A. P. Fein, *Proc. SPIE* **4608**, 112 (2002).
- G. M. Rutter *et al.*, *Nat. Phys.* **7**, 649 (2011).
- D. L. Miller *et al.*, *Science* **324**, 924 (2009).
- G. Li, A. Luican, E. Y. Andrei, *Phys. Rev. Lett.* **102**, 176804 (2009).
- Additional supplementary text and data are available on *Science Online*.
- B. J. LeRoy, J. Kong, V. K. Pahilwani, C. Dekker, S. G. Lemay, *Phys. Rev. B* **72**, 075413 (2005).
- L. P. Kouwenhoven, D. G. Austing, S. Tarucha, *Rep. Prog. Phys.* **64**, 701 (2001).

- We determined the 1 SD error estimates in the QD sizes by combining the 1 SD in the addition energy variation for the first and last set of energies in Fig. 3G, together with the 1 SD uncertainties in the measured slopes of the charging lines in the gate maps.
- M. I. Katsnelson, K. S. Novoselov, A. K. Geim, *Nat. Phys.* **2**, 620 (2006).
- J. Güttinger *et al.*, *Phys. Rev. Lett.* **103**, 046810 (2009).

Acknowledgments: We thank M. Stiles and S. Adam for valuable discussions and S. Blankenship and A. Band for technical assistance. The U.S. National Science Foundation is gratefully acknowledged via grants CMMI-1069076 and CMMI-1129826 (T.L. and S.Z.) and grant CMMI-0841840 (C.A.W. and S.D.S.).

Supplementary Materials

www.sciencemag.org/cgi/content/full/336/6088/1557/DC1
Supplementary Text
Figs. S1 to S13
References (24–26)
9 February 2012; accepted 30 April 2012
10.1126/science.1220335

Electrical Wind Force–Driven and Dislocation-Templated Amorphization in Phase-Change Nanowires

Sung-Wook Nam,^{1*} Hee-Suk Chung,^{1*} Yu Chieh Lo,^{1,2} Liang Qi,^{1,2} Ju Li,^{1,2} Ye Lu,³ A.T. Charlie Johnson,^{1,3} Yeonwoong Jung,¹ Pavan Nukala,¹ Ritesh Agarwal^{1†}

Phase-change materials undergo rapid and reversible crystalline-to-amorphous structural transformation and are being used for nonvolatile memory devices. However, the transformation mechanism remains poorly understood. We have studied the effect of electrical pulses on the crystalline-to-amorphous phase change in a single-crystalline $\text{Ge}_2\text{Sb}_2\text{Te}_5$ (GST) nanowire memory device by *in situ* transmission electron microscopy. We show that electrical pulses produce dislocations in crystalline GST, which become mobile and glide in the direction of hole-carrier motion. The continuous increase in the density of dislocations moving unidirectionally in the material leads to dislocation jamming, which eventually induces the crystalline-to-amorphous phase change with a sharp interface spanning the entire nanowire cross section. The dislocation-templated amorphization explains the large on/off resistance ratio of the device.

Chalogenide-based phase-change memory (PCM) materials have been widely used for optical data storage and are now finding applications in electronic memory devices (1, 2). In a nonvolatile PCM device, the difference in optical reflectivity or electrical resistance between amorphous and crystalline phases is used to store information. Memory switching is performed by applying optical (or electrical) pulses: short pulses with large amplitude to amorphize the material and long pulses

with low amplitude for the crystallization process. It has been generally assumed that the large amplitude of the pulse melts the material, and its short duration locks the atoms in their disordered positions owing to rapid quenching. The understanding of the effects of electric field on the crystalline-to-amorphous phase transition in PCM is critical for designing low-power nonvolatile memory devices. Therefore, it is desirable to visualize and characterize the critical events that lead to the phase-change process while the device is under operation, which can uncover phenomena that cannot be gleaned from *ex situ* measurements (3). However, it is challenging to resolve the amorphization phenomena with high spatial and/or temporal resolution in confined structures such as in conventional thin-film devices with a sandwich geometry (4). Very recently, based on time-resolved photo-excitation measurements of PCM materials (5, 6), it has been argued that the material did not amorphize

via the liquid-state pathway, but by a solid-state, lattice-distortion-triggered process. Consequently, visualization of the structural evolution of the PCM device under electrical biasing by correlating it to the electrical-resistance variation would be helpful. A single-crystalline device can serve as an ideal platform to study the relationship between microstructural evolution and electrical resistance variation, so as to avoid the effects of preexisting grain boundaries on carrier transport and structural dynamics. In conventional PCM devices, polycrystalline thin films with relatively small grain sizes (10 to 20 nm) preclude the visualization of switching behavior originating from single grains. By using the single-crystalline, lateral, and open geometry of the $\text{Ge}_2\text{Sb}_2\text{Te}_5$ (GST) nanowire structure, we visualized the amorphization behavior and found it to be critically associated with the nucleation and dynamics of dislocations.

We assembled GST nanowire memory devices across 2-μm-wide trenches fabricated on a thin silicon-nitride membrane (Fig. 1A) to enable real-time visualization of nanoscale structural changes with high spatial resolution under the influence of applied electrical voltage pulses inside a transmission electron microscope (TEM) (figs. S1 to S4) (7). Single-crystalline GST nanowires with hexagonal crystal structure grown along the [1010] axis were synthesized through the vapor-liquid-solid method (fig. S1) (8). For device operation, voltage pulses with duration of a few hundred nanoseconds were applied, and between each pulse, the resistance was measured at a DC bias of 0.2 V (Fig. 1B). We note that all the reported electrical resistances in this paper are not the dynamic resistances during electrical pulsing, but the stationary resistance values of the devices measured long after the pulsing process so that the heat generated during the pulsing was dissipated and the devices reached room temperature. The resistance (after each 300-ns pulse with increasing voltage amplitude)

¹Department of Materials Science and Engineering, University of Pennsylvania, Philadelphia, PA 19104, USA. ²Department of Nuclear Science and Engineering and Department of Materials Science and Engineering, Massachusetts Institute of Technology, Cambridge, MA 02139, USA. ³Department of Physics and Astronomy, University of Pennsylvania, Philadelphia, PA 19104, USA.

*These authors contributed equally to this work.

†To whom correspondence should be addressed. E-mail: riteshag@seas.upenn.edu

Supplementary Materials for

Electromechanical Properties of Graphene Drumheads

Nikolai N. Klimov, Suyong Jung, Shuze Zhu, Teng Li,* C. Alan Wright, Santiago D. Solares,* David B. Newell, Nikolai B. Zhitenev, Joseph A. Stroscio*

*To whom correspondence should be addressed. E-mail: ssolares@umd.edu (S.D.S.); lit@umd.edu (T.L.); joseph.stroscio@nist.gov (J.A.S.)

Published 22 June 2012, *Science* **336**, 1557 (2012)

DOI: 10.1126/science.1220335

This PDF file includes:

- Supplementary Text
- Figs. S1 to S13
- Full Reference List

I. COMPARISON OF TUNNELING SPECTROSCOPY OF GRAPHENE SUPPORTED ON SiO₂ VS. SUSPENDED GRAPHENE

Gate mapping tunneling spectroscopy measurements of suspended graphene are very different from measurements of graphene supported on SiO₂ substrates (Fig. S1). The spectroscopic measurements of supported graphene at $B = 0$ T are characterized by a minimum in the differential conductance at the Dirac point (13). The position of the Dirac point in zero magnetic field varies in energy as a function of gate voltage as shown by the dashed line in Fig. S1A. The variation of the Dirac point is given by, $E_D = \hbar v_F \sqrt{\pi n}$, where v_F is the Fermi velocity of graphene, and $n = \alpha |V_{GATE} - V_0|$ is the two-dimensional (2D) charge-carrier density induced by the applied gate potential V_{GATE} . V_0 is the shift of the Dirac point created by local intrinsic doping, and $\alpha = 7.19 \times 10^{10} \text{ cm}^{-2} \text{ V}^{-1}$ for the 300 nm thickness of the SiO₂ substrate layer on Si. Following the Dirac point variation with gate voltage are a series of resonances observed as small peaks in the dI/dV measurements, which are due to scattering in the disorder potential from the underlying substrate (13, 24). As a magnetic field is applied, the supported graphene measurements display a new discrete state at the Dirac point, the $N=0$ Landau level, LL₀ (Fig. S1B). In addition to the appearance of LL₀, the Dirac point variation with gate voltage now shows a staircase-like dependence on gate voltage instead of the ideal square-root variation. The staircase-like steps are due to the pinning of the Fermi level as each Landau level, LL_N, is filled as the gate voltage is increased (Fig. S1B). The effect of the disorder potential in the applied magnetic field is to form a spatial landscape of compressible (metallic) and incompressible (insulating) regions, depending on the position of the LL with respect to the Fermi level. When a compressible region is located under the tunneling region that is surrounded by insulating incompressible regions, the quantum dot-like charging resonances are observed in the dI/dV gate maps as near vertical lines intersecting LLs at the Fermi level (Fig. S1B). For graphene these lines come in groups of four due to the four-fold degeneracy of electron spin and valley quantum numbers, and can be seen at a gate voltage of 19 V for LL₀ and 28 V for LL₁ in Fig. S1B. The charging resonances reflect a new tunneling channel opening up when the quantum dot energy levels line up with the Fermi level of the sample under the influence of the combined gate voltage (horizontal axis) and tunneling voltage (vertical axis).

The tunneling spectroscopy measurements on suspended graphene can be directly compared to supported graphene, by comparing Figs. S1, C and D, with Figs. S1, A and B. In zero applied magnetic field, a distinct minimum corresponding to the Dirac point can no longer be identified on the suspended graphene. The gate mapping measurements (Fig. S1C) show a series of new peaks with a weak negative slope with respect to gate voltage, and broader bands with a strong positive slope, instead of the Dirac minimum in the zero field case. The positive slope bands become split into four separate lines in an applied magnetic field (Fig. S1D). We interpret this spectrum as a signature of a graphene quantum dot produced by spatial confinement in a strain-induced pseudomagnetic field, which spatially alternates in sign (see main text and simulations below). The confinement is enhanced by an applied external magnetic field, and the

sharper four-fold peaks indicate a longer lifetime and hence less leakage of the states in the QD.

The positive slope lines in the gate map of the suspended graphene (Fig. S1D) resemble the charging lines observed on the supported graphene (Fig. S1B). However, the overall behavior is quite different in these two cases. Briefly, the main characteristics of charging phenomena on supported graphene are: 1) the QDs are formed around spatial positions of density minima and maxima determined by a frozen disorder potential; 2) QDs are defined only in large magnetic fields bounded by spatial areas of vanishing density of states (resistive “incompressible” strips or strips with nearly integer filling factors; 3) as a consequence, at a given spatial location, a QD exists at a fixed filling factor meaning that the charging lines on gate maps shift with magnetic field. For example, the lines that intersect LL₁ at 28 V for $B=5$ T in Fig. S1B will be at a different gate voltage for a different field; and 4) details of the QDs evolution are clearly distinct for density minima and maxima (see ref. 13 supplemental material).

In the case of the current experiment on suspended graphene we observe that: 1) QDs exist already in zero magnetic field. Large magnetic fields only strengthens the localization and increases the lifetimes making the charging lines narrower and hence more visible, 2) the position of the charging lines on the gate maps is *unaffected* by magnetic fields, and 3) the QD tracks the position of the tip and is not fixed spatially by the disorder landscape.

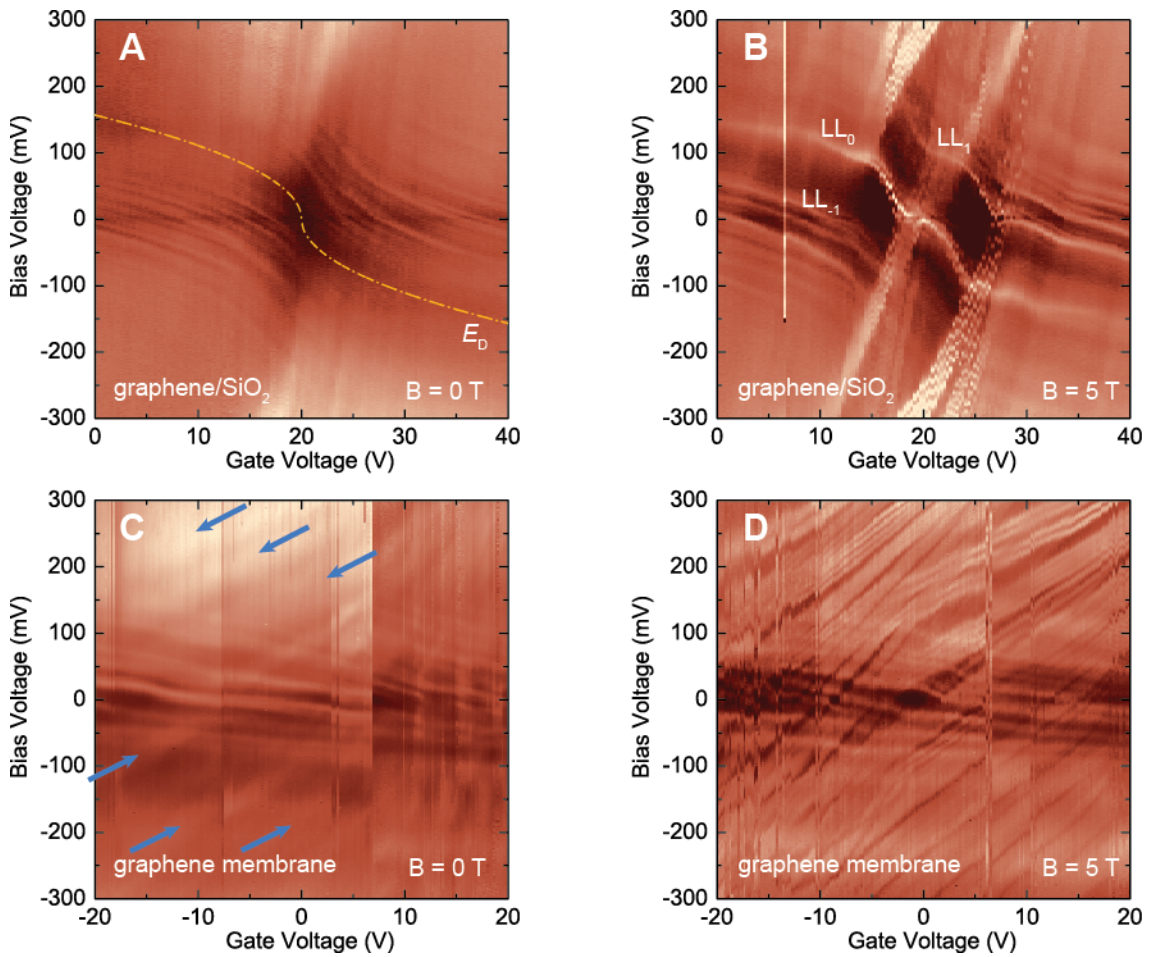


Figure S1. A comparison of gate mapping scanning tunneling spectroscopy of supported and suspended graphene. (A,B) dI/dV gate map spectra on graphene supported on SiO_2/Si substrate at $B = 0 \text{ T}$ and $B = 5 \text{ T}$, respectively. The yellow dash-dotted line in (A) shows the evolution of the Dirac point at 0 T as a function of gate voltage. Landau levels are formed in the supported graphene in an applied magnetic field. The three lowest Landau levels (LL_0 , $LL_{\pm 1}$) are marked on (B). (C,D) dI/dV gate map spectra on suspended graphene membrane at $B = 0 \text{ T}$ and $B = 5 \text{ T}$, respectively. The blue arrows in (C) indicate quantum dot charging bands that become more pronounced in an applied magnetic field (D). The color scale on gate maps indicates the dI/dV magnitude ranging from 0.05 nS to 1.2 nS (A, B, D), and from 0.05 nS to 1.7 nS for (C); lighter color corresponds to larger dI/dV magnitude.

Below we summarize the simulation methods and results on the interaction of iridium STM probe tips and suspended graphene membranes. The simulation results are organized by modeling technique. Section II: quantum mechanics simulations (QM), III: molecular dynamics simulations (MD), and IV: scaling analysis of the van der Waals force range vs. probe tip radius. Overviews of the key results are provided in each case.

II. QUANTUM MECHANICS SIMULATIONS

The purpose of these calculations was to identify possible electronic structure changes in the graphene membrane as a result of its interaction with the iridium STM tip. The calculations were conducted using the SeqQuest Density Functional Theory (DFT) code developed at Sandia National Laboratory (<http://dft.sandia.gov/Quest/>), within the PBE functional of the generalized gradient approximation (GGA). A double-zeta basis set with polarization functions was used. All calculations are full minimizations of the geometry, keeping only the top layer of the STM tip and the edge membrane atoms fixed.

Two crystal orientations were considered for the STM tip, namely Ir(100) and Ir(111) (Figure S2). For each tip, tip-membrane approach curves were calculated at the locations indicated in Figure S3. The graphene sheet was terminated with hydrogen and oxygen atoms, as needed, in order to retain the SP² character for all carbon atoms in the system. All edge (H and O) atoms were kept fixed during the calculations.

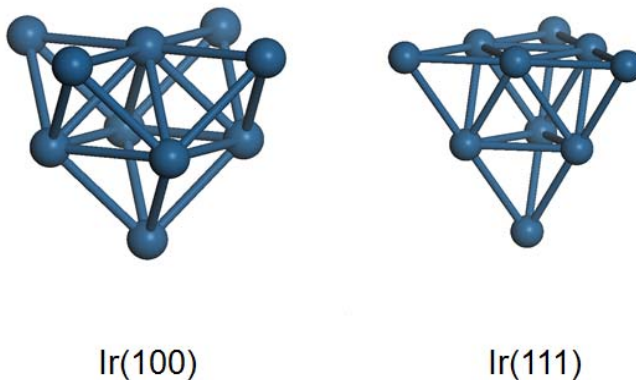


Figure S2. Atomistic models of the STM tip used in the quantum mechanics calculations.

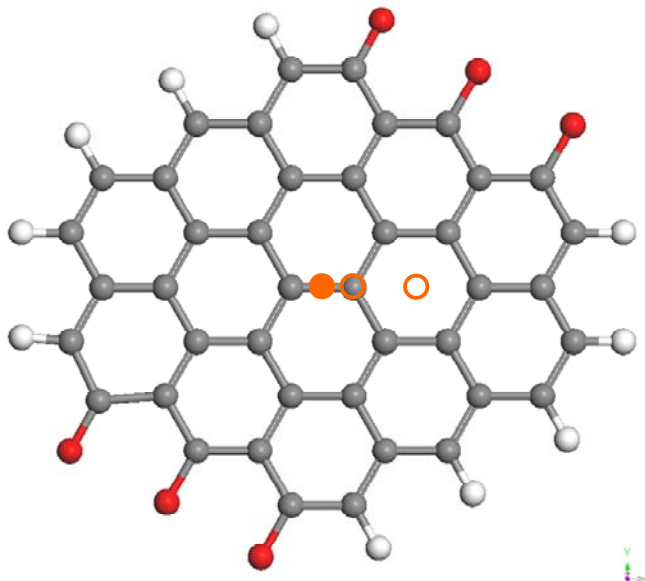


Figure S3. Graphene structure modeled in the quantum mechanics calculations. Carbon atoms are shown in gray, oxygen in red and hydrogen in white. Hydrogen and oxygen atoms are used to terminate the structure such that all carbon atoms remain planar (sp^2). The orange markers indicate the locations where approach curves were calculated: C-C bond, C atom and ring center.

Figure S4 shows typical geometry changes observed during the approach curves. These results are for the Ir(100) tip, but are typical of all curves conducted with both tip orientations at all three locations shown in Figure S3. The images depict how the membrane is initially attracted towards the tip and deforms despite its small size and high tension due to being fixed at the edges.

Figure S5 shows the evolution of the differential electronic density of the Ir(100)/graphene system upon approach (the differential electronic density is the difference between the final converged density and the initial guess of the software, which treats all atoms of a given element as being identical). Initially the density at the tip apex exhibits four-fold symmetry in the attractive tip-sample force regime (this is where STM experiments are conducted), which changes to two-fold when the interaction becomes repulsive.

Figure S6 compares the differential electronic density to the total electronic density (the former is easier to visualize) and Figure S7 compares the differential electronic density for the Ir(100)/graphene and Ir(111)/graphene systems.

The main conclusion of these results is that no changes in graphene atom character are observed.

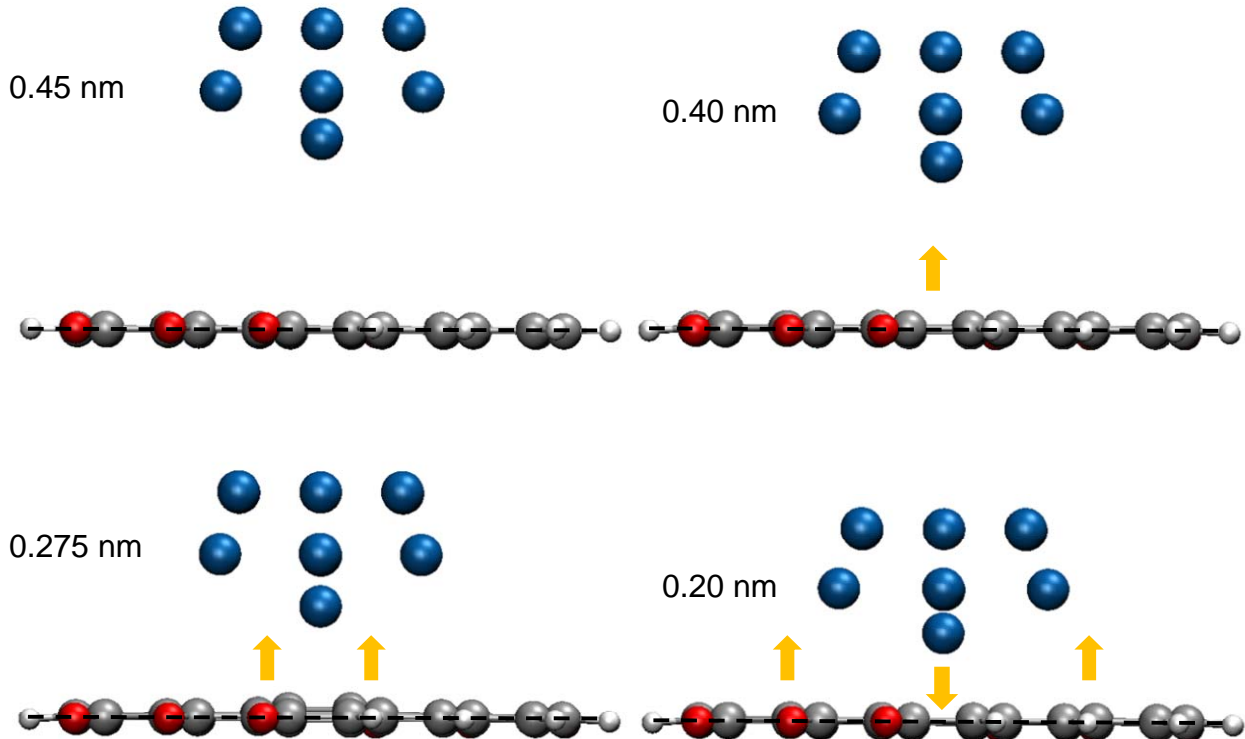


Figure S4. Typical displacements of the graphene membrane during the approach of the iridium tip. The images shown are for the Ir(100) tip approaching the location designated as C-C bond in Figure S3, but the results obtained for Ir(111) and at other locations were qualitatively similar. The membrane does not deform appreciably when the tip is ~ 0.4 nm or more away from the surface. Below this position the membrane initially undergoes attraction from the tip's front atom, and then simultaneous repulsion from the tip's front atom and attraction from the tip's second layer. No significant changes were observed in the character of the carbon atoms.

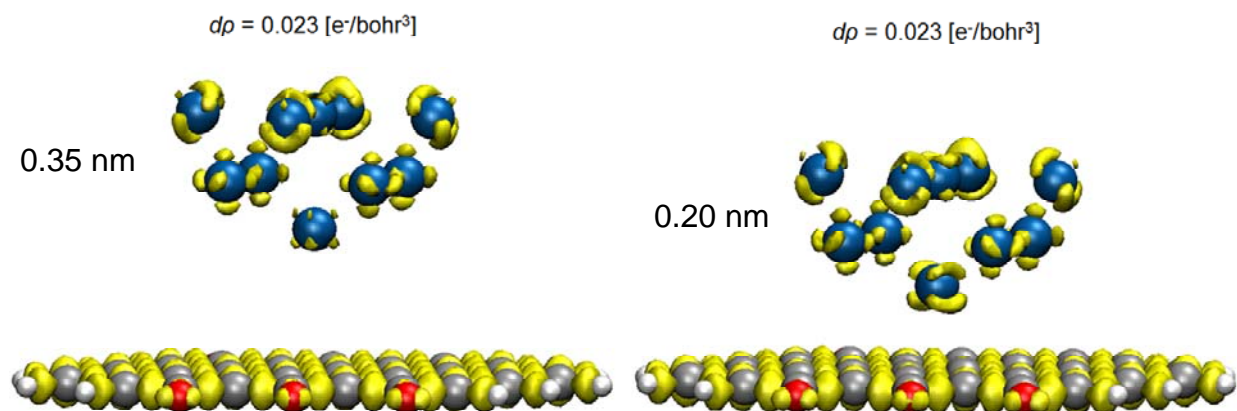


Figure S5. Evolution of the electronic density of the Ir(100) tip as it approaches the sample. Four-fold symmetry is observed in the attractive tip-sample force regime, which changes to 2-fold symmetry in the repulsive regime. This image shows the change in

density of the system between the initial DFT iteration, where all atoms of a given element are identical, and the final minimized iteration where the system's energy is at a minimum. The differences in the change in density are easier to visualize than the differences in the total density (see Figure S6).

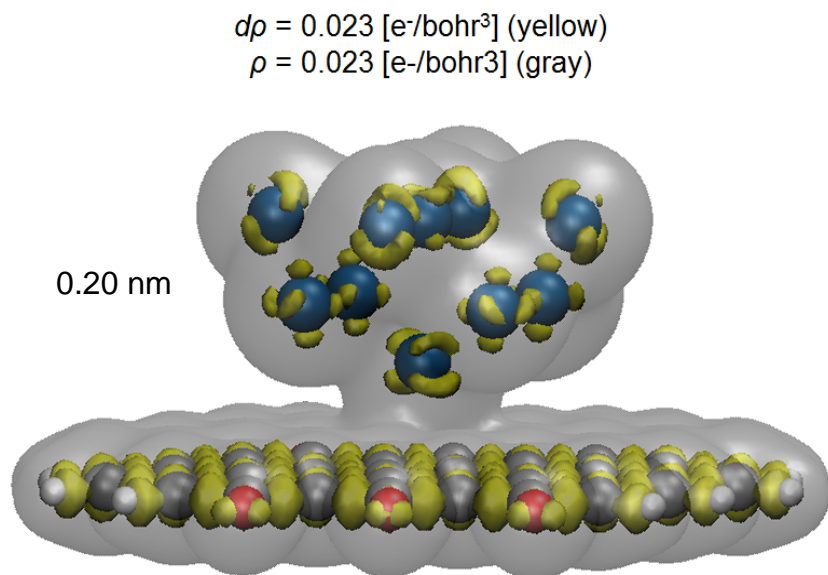


Figure S6. Comparison of the change in electronic density shown in Figure S5 with the total electronic density of the system for the Ir(100)/graphene system.

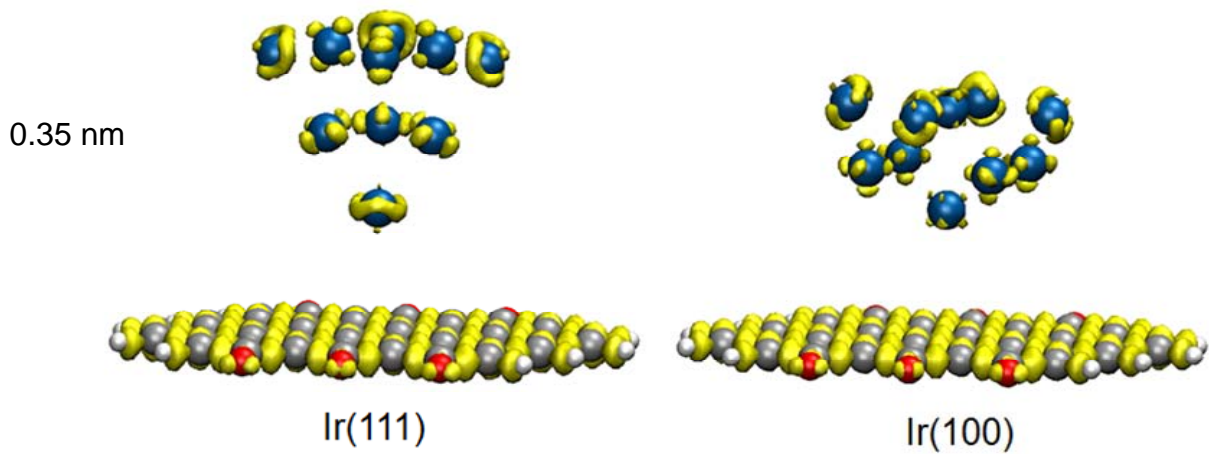


Figure S7. Comparison of the change in electronic density for the Ir(111) and Ir(100) tips.

III. MOLECULAR DYNAMICS SIMULATIONS

The molecular dynamics (MD) simulations were conducted using the LAMMPS simulator developed at Sandia National Laboratory (<http://lammps.sandia.gov/>).

The crystal structure of iridium is Face-Centered Cubic (FCC) with lattice constant of 0.384 nm. The STM tip was initially modeled as a hemisphere, as shown in Figure S8. The top surface of this tip is oriented in the [100] direction, although the effect of crystal orientation is negligible at the MD length scale considered.

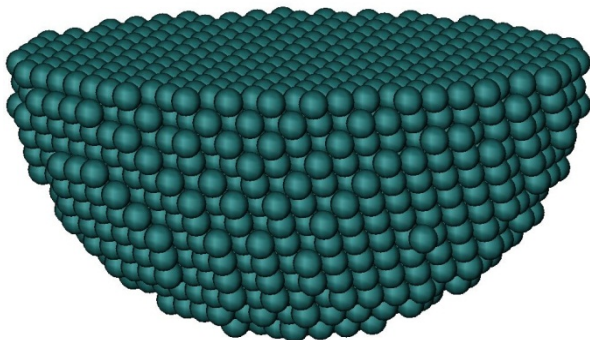


Figure S8. Atomistic model of iridium STM tip in MD simulations.

The nonbonded interaction between iridium and carbon atoms was modeled using a Lennard-Jones (LJ) 6-12 potential. The parameters were developed through the customary Lorentz-Berthelot mixing rules, using Ir-Ir and C-C parameters from the Universal Force Field (25). The AIREBO potential (26) was used to model the interaction of the carbon atoms within the graphene membrane (including the C-C nonbonded parameters). The atomic interactions within the iridium tip itself were not included since geometrical changes in the tip are expected to have a negligible effect at the length scale under consideration. The tip/membrane model was scaled down from the experimental system to reduce computational expense. Thus, a tip radius of 2.5 nm and a graphene membrane radius of 25.0 nm were used.

Simulations were conducted for three horizontal tip locations with respect to the membrane: 2.5 nm from the edge, 5.2 nm from the edge and the center of the membrane. In each case, the simulation began with the tip pressed down into the membrane. The tip was gradually retracted from the membrane in increments of 0.006 nm while the membrane was allowed to relax at a temperature of 5 K. The membrane initially maintained contact with the tip, but eventually a critical point was reached at which the membrane could no longer maintain contact with the tip. The geometry for this critical height was then optimized to absolute zero. Finally, to obtain higher resolution in the membrane height, zero Kelvin calculations were conducted in which the tip was raised further from this optimized geometry in increments of 0.001 nm until tip-membrane

contact could not be sustained. This provided the equilibrium membrane geometries for the critical heights at the three horizontal tip locations. This exercise was repeated for different levels of “gate force,” which was simulated by applying a downward force of equal magnitude to each atom of the membrane. The force applied to each atom ranged from 0 to 0.06 pN per atom. Shown in Figure S9 is the effect of the applied force level on the critical membrane shape for the case of the tip above the center of the membrane. The red profile corresponds to zero force. The blue, black, and green profiles correspond to downward forces of 0.012, 0.037, and 0.061 pN per atom, respectively.

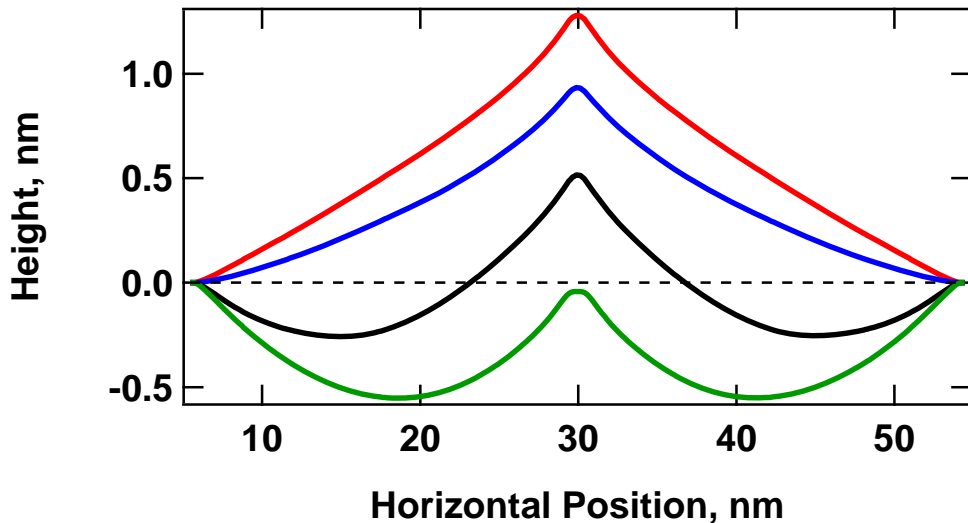


Figure S9. The effect of the applied downward force on the calculated membrane shapes for the case of the tip above the center of the membrane. The profiles, from top to bottom, correspond to applied forces of 0, 0.012, 0.037, and 0.061 pN per atom, respectively.

The per-atom stress values obtained from LAMMPS were used to calculate the per-atom strain for a given equilibrium membrane geometry by utilizing the constitutive equations for a linear isotropic material. LAMMPS uses a stress*volume formulation, which means that the computed quantity is in units of pressure*volume. Thus, calculated values must be scaled by the effective per-atom volume. Figure S10 shows the strain components u_{xx} , u_{yy} , and u_{xy} used to calculate the pseudomagnetic field of Figure 4 in the paper. To calculate the pseudomagnetic field, the pseudogauge field $\mathbf{A}_{ps}(\mathbf{r})$ is calculated as (4, 6),

$$\mathbf{A}_{ps} = \frac{t\beta}{ev_F} (u_{xx} - u_{yy}, -2u_{xy}), \quad (1)$$

where we take the dimensionless coupling constant $\beta=2.5$, the hopping energy $t=2.8$ eV, and the Fermi velocity $v_F=1\times 10^6$ m s⁻¹. The pseudomagnetic field is given by

$\mathbf{B}_{ps} = \nabla \times \mathbf{A}_{ps}$ and is shown in Fig. 4B of the main text.

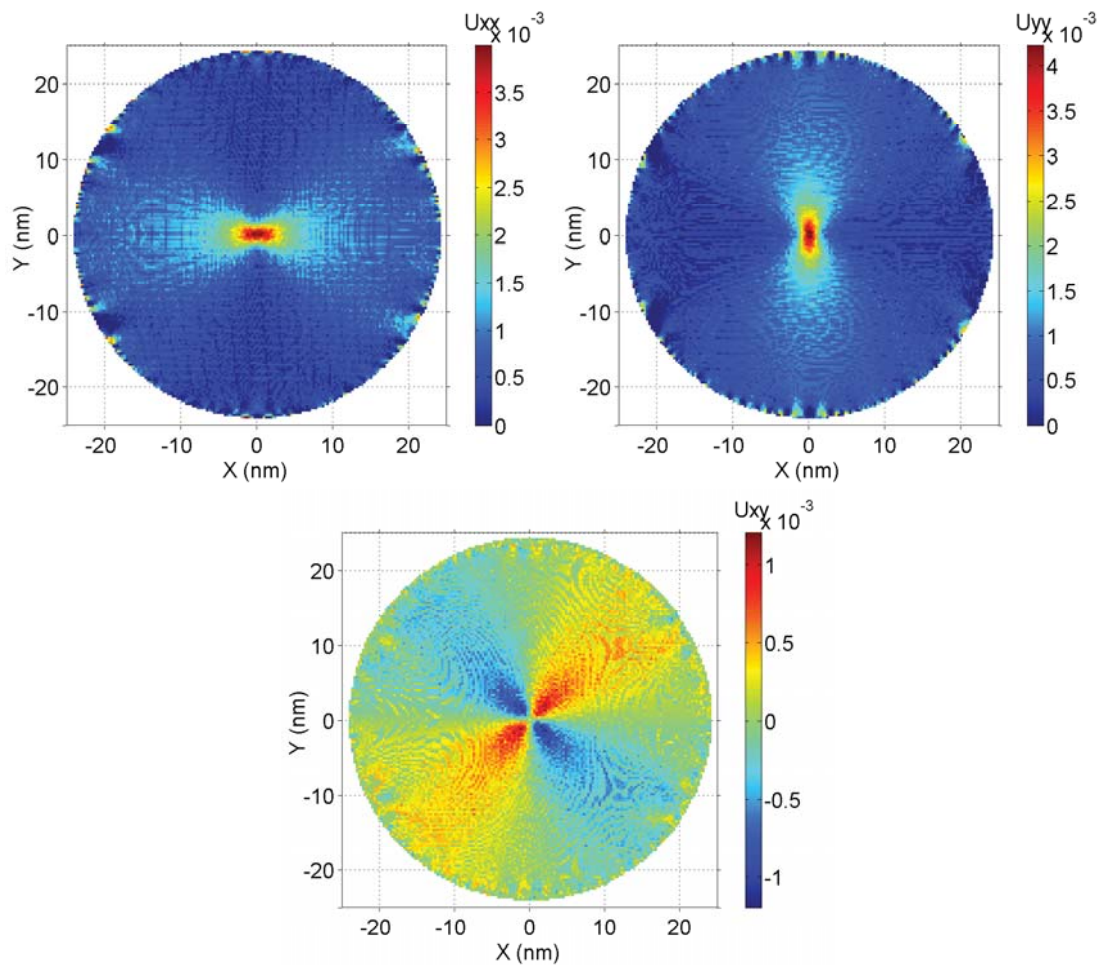


Figure S10. Strain components (A) u_{xx} (B) u_{yy} , and (C) u_{xy} as calculated from the per-atom stresses in LAMMPS for the tip over the center of the membrane with zero applied force. These strain components were used to calculate the pseudomagnetic field discussed in the paper.

IV. SCALING ANALYSIS OF THE VAN DER WAALS FORCE VS. PROBE TIP RADIUS

We also conducted calculations to estimate the approximate size of the “spot” on the graphene membrane on which the tip exerts an attractive force, as a function of the tip radius. To carry out this estimate we begin with the equation describing the non-bonded interaction energy between a C atom and an Ir atom, which is given by the Lennard-Jones Potential,

$$E_{C-Ir}(d) = \frac{A}{d^{12}} - \frac{B}{d^6} \quad (2)$$

where A and B are constants and d is the distance between the centers of the atoms. We now consider a single carbon atom interacting with an iridium sphere representing the STM tip. To calculate the interaction potential, we perform an integration of the interaction energy over the volume of the iridium sphere,

$$E_{C-Ir_sphere}(D) = \int_0^{2\pi} \int_0^{\pi} \int_0^R N E(d(D, r, \theta, \phi)) r^2 \sin(\theta) dr d\theta d\phi \quad (3)$$

where E_{C-Ir_sphere} is the interaction energy between the Ir sphere and a C atom located at a distance D from the surface of the sphere, N is the number density of bulk Ir, d is the distance between the differential volume element in the Ir sphere ($r^2 dr d\theta d\phi$) and the C atom, and E is the C-Ir interaction potential given by equation (2). We now imagine that we place spheres of different sizes above the center of a flat, circular graphene membrane. We assume that the spheres have been placed at a height for which the force exerted on an atom located on the center of the membrane is zero (see Figure S11), and plot the force between the Ir sphere and single C atoms located a different distances from the center. The results for different tip radii are shown in Figures S12 and S13. The direction of the force is towards the center of the tip sphere, which is close to the upward normal direction due to the relatively large tip radius compared to the horizontal range of the force, especially for the larger tip sizes. The results show that the range of the force increases with the *square root* of the tip radius, which is evident in Figure S13, in which the forces for three of the cases shown in Figure S12 have been plotted against axes that have been rescaled according to the square root of the tip radius.

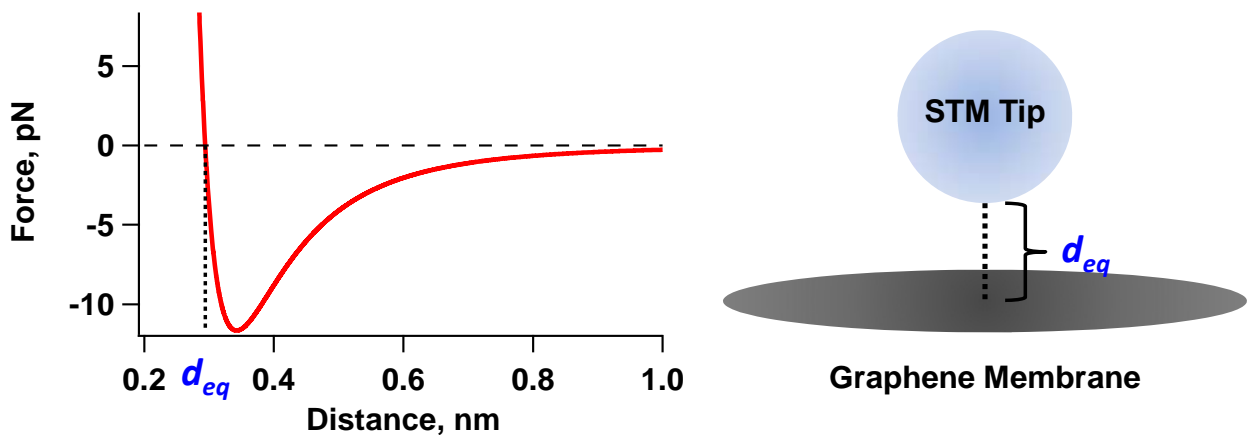


Figure S11. (left) Interaction force curve describing the force exerted by a 50 nm Ir sphere on a single C atom. The distance corresponds to the separation between the C atom center and the skin of the sphere. d_{eq} denotes the tip-atom separation for which the force is zero.

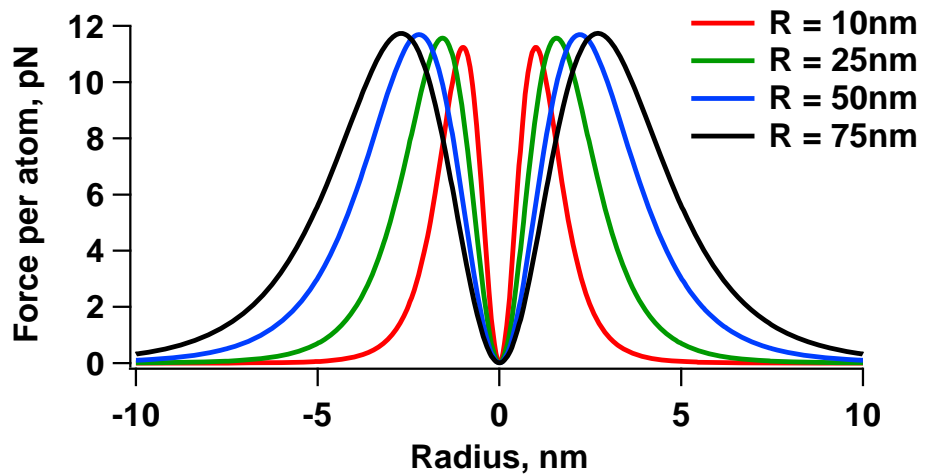


Figure S12. Magnitude of the force exerted by the Ir tip on a single C atom on the graphene membrane as a function of the atom's horizontal distance from the membrane center and the tip radius of curvature. The direction of the force is toward the center of the Ir sphere (see Figure S11).

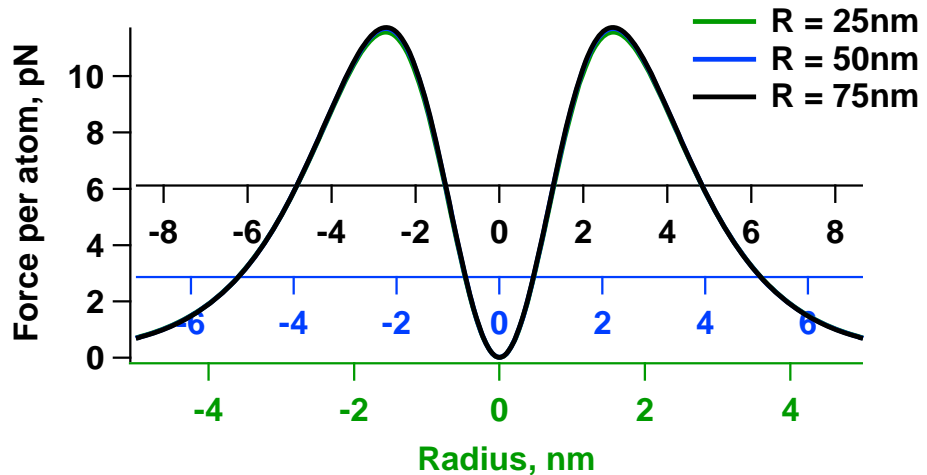


Figure S13. Similar plots as those of Figure S12, but rescaling the horizontal axes by the square root of the tip radius in each case (for clarity only three cases are included). The curves fall almost on top of each other.

References and Notes

1. K. S. Novoselov *et al.*, Two-dimensional atomic crystals. *Proc. Natl. Acad. Sci. U.S.A.* **102**, 10451 (2005). [doi:10.1073/pnas.0502848102](https://doi.org/10.1073/pnas.0502848102) Medline
2. K. I. Bolotin *et al.*, Ultrahigh electron mobility in suspended graphene. *Solid State Commun.* **146**, 351 (2008). [doi:10.1016/j.ssc.2008.02.024](https://doi.org/10.1016/j.ssc.2008.02.024)
3. M. M. Fogler, F. Guinea, M. I. Katsnelson, Pseudomagnetic fields and ballistic transport in a suspended graphene sheet. *Phys. Rev. Lett.* **101**, 226804 (2008). [doi:10.1103/PhysRevLett.101.226804](https://doi.org/10.1103/PhysRevLett.101.226804) Medline
4. F. Guinea, M. I. Katsnelson, A. K. Geim, Energy gaps and a zero-field quantum Hall effect in graphene by strain engineering. *Nat. Phys.* **6**, 30 (2010). [doi:10.1038/nphys1420](https://doi.org/10.1038/nphys1420)
5. N. Levy *et al.*, Strain-induced pseudo-magnetic fields greater than 300 tesla in graphene nanobubbles. *Science* **329**, 544 (2010). [doi:10.1126/science.1191700](https://doi.org/10.1126/science.1191700) Medline
6. K.-J. Kim, Y. M. Blanter, K.-H. Ahn, Interplay between real and pseudomagnetic field in graphene with strain. *Phys. Rev. B* **84**, 081401 (2011). [doi:10.1103/PhysRevB.84.081401](https://doi.org/10.1103/PhysRevB.84.081401)
7. G. M. M. Wakker, R. P. Tiwari, M. Blaauboer, Localization and circulating currents in curved graphene devices. *Phys. Rev. B* **84**, 195427 (2011). [doi:10.1103/PhysRevB.84.195427](https://doi.org/10.1103/PhysRevB.84.195427)
8. F. Guinea, B. Horovitz, P. Le Doussal, Gauge field induced by ripples in graphene. *Phys. Rev. B* **77**, 205421 (2008). [doi:10.1103/PhysRevB.77.205421](https://doi.org/10.1103/PhysRevB.77.205421)
9. F. Guinea, A. K. Geim, M. I. Katsnelson, K. S. Novoselov, Generating quantizing pseudomagnetic fields by bending graphene ribbons. *Phys. Rev. B* **81**, 035408 (2010). [doi:10.1103/PhysRevB.81.035408](https://doi.org/10.1103/PhysRevB.81.035408)
10. T. O. Wehling, A. V. Balatsky, A. M. Tsvelik, M. I. Katsnelson, A. I. Lichtenstein, Midgap states in corrugated graphene: Ab initio calculations and effective field theory. *Europhys. Lett.* **84**, 17003 (2008). [doi:10.1209/0295-5075/84/17003](https://doi.org/10.1209/0295-5075/84/17003)
11. M. Gibertini, A. Tomadin, M. Polini, Electron density distribution and screening in rippled graphene sheets. *Phys. Rev. B* **81**, 125437 (2010). [doi:10.1103/PhysRevB.81.125437](https://doi.org/10.1103/PhysRevB.81.125437)
12. S. Jung *et al.*, Evolution of microscopic localization in graphene in a magnetic field from scattering resonances to quantum dots. *Nat. Phys.* **7**, 245 (2011). [doi:10.1038/nphys1866](https://doi.org/10.1038/nphys1866)
13. A. Luican, G. Li, E. Y. Andrei, Quantized Landau level spectrum and its density dependence in graphene. *Phys. Rev. B* **83**, 041405 (2011). [doi:10.1103/PhysRevB.83.041405](https://doi.org/10.1103/PhysRevB.83.041405)
14. J. A. Stroscio, E. W. Hudson, S. R. Blankenship, R. J. Celotta, A. P. Fein, Facility for nanoscience research: An overview. *Proc. SPIE* **4608**, 112 (2002). [doi:10.1117/12.438493](https://doi.org/10.1117/12.438493)
15. G. M. Rutter *et al.*, Microscopic polarization in bilayer graphene. *Nat. Phys.* **7**, 649 (2011). [doi:10.1038/nphys1988](https://doi.org/10.1038/nphys1988)
16. D. L. Miller *et al.*, Observing the quantization of zero mass carriers in graphene. *Science* **324**, 924 (2009). [doi:10.1126/science.1171810](https://doi.org/10.1126/science.1171810) Medline
17. G. Li, A. Luican, E. Y. Andrei, Scanning tunneling spectroscopy of graphene on graphite. *Phys. Rev. Lett.* **102**, 176804 (2009). [doi:10.1103/PhysRevLett.102.176804](https://doi.org/10.1103/PhysRevLett.102.176804) Medline

18. Additional supplementary text and data are available on *Science* Online.
19. B. J. LeRoy, J. Kong, V. K. Pahilwani, C. Dekker, S. G. Lemay, Three-terminal scanning tunneling spectroscopy of suspended carbon nanotubes. *Phys. Rev. B* **72**, 075413 (2005). [doi:10.1103/PhysRevB.72.075413](https://doi.org/10.1103/PhysRevB.72.075413)
20. L. P. Kouwenhoven, D. G. Austing, S. Tarucha, Few-electron quantum dots. *Rep. Prog. Phys.* **64**, 701 (2001). [doi:10.1088/0034-4885/64/6/201](https://doi.org/10.1088/0034-4885/64/6/201)
21. We determined the 1 SD error estimates in the QD sizes by combining the 1 SD in the addition energy variation for the first and last set of energies in Fig. 3G, together with the 1 SD uncertainties in the measured slopes of the charging lines in the gate maps.
22. M. I. Katsnelson, K. S. Novoselov, A. K. Geim, Chiral tunnelling and the Klein paradox in graphene. *Nat. Phys.* **2**, 620 (2006). [doi:10.1038/nphys384](https://doi.org/10.1038/nphys384)
23. J. Güttinger *et al.*, Electron-hole crossover in graphene quantum dots. *Phys. Rev. Lett.* **103**, 046810 (2009). [doi:10.1103/PhysRevLett.103.046810](https://doi.org/10.1103/PhysRevLett.103.046810) [Medline](#)
24. C. E. Malec, D. Davidović, Transport in graphene tunnel junctions. *J. Appl. Phys.* **109**, 064507 (2011). [doi:10.1063/1.3554480](https://doi.org/10.1063/1.3554480)
25. A. K. Rappe, C. J. Casewit, K. S. Colwell, W. A. Goddard, W. M. Skiff, UFF, a full periodic table force field for molecular mechanics and molecular dynamics simulations. *J. Am. Chem. Soc.* **114**, 10024 (1992). [doi:10.1021/ja00051a040](https://doi.org/10.1021/ja00051a040)
26. S. J. Stuart, A. B. Tutein, J. A. Harrison, A reactive potential for hydrocarbons with intermolecular interactions. *J. Chem. Phys.* **112**, 6472 (2000). [doi:10.1063/1.481208](https://doi.org/10.1063/1.481208)